

Development of laser heterodyne photothermal displacement method for mapping carrier nonradiative recombination centers in semiconductors

Cite as: J. Appl. Phys. **131**, 195701 (2022); doi: [10.1063/5.0085041](https://doi.org/10.1063/5.0085041)

Submitted: 12 January 2022 · Accepted: 26 April 2022 ·

Published Online: 17 May 2022



Tomoki Harada,^{1,2}  Tetsuo Ikari,¹  and Atsuhiko Fukuyama^{1,a)} 

AFFILIATIONS

¹Faculty of Engineering, University of Miyazaki, 1-1 Gakuen-Kibanadai-Nishi, Miyazaki 889-2192, Japan

²Research Fellow of Japan Society for the Promotion of Science, Kojimachi Business Center Building, 5-3-1 Kojimachi, Chiyoda-ku, Tokyo 102-0083, Japan

^{a)}Author to whom correspondence should be addressed: a-fukuyama@cc.miyazaki-u.ac.jp

ABSTRACT

The laser heterodyne photothermal displacement (LH-PD) method was used to characterize the nonradiative recombination centers of semiconductors, such as defects and deep-lying electronic levels. When a semiconductor surface is irradiated with a modulated continuous wave laser, the irradiated area is periodically heated and expanded owing to the nonradiative recombination of the photoexcited carriers. The LH-PD can measure an absolute value of surface displacement and its time variation at various excitation beam frequencies (f_{ex}). Si and GaAs substrate samples were used to confirm the usefulness of the proposed method. The obtained time variation of the surface displacement was well explained by theoretical calculations considering the carrier generation, diffusion, recombination, heat diffusion, and generated thermal strain. Because nonradiative carrier recombination generates local heat at defects in semiconductors, the LH-PD technique is useful for analyzing defect distributions. Additionally, measurements of intentional Fe-contaminated Si samples confirmed that this technique is suitable for defect mapping. Displacement mapping with changing f_{ex} suggests the potential to measure the distribution of non-radiative recombination centers in the sample depth direction.

Published under an exclusive license by AIP Publishing. <https://doi.org/10.1063/5.0085041>

I. INTRODUCTION

Photothermal methods have been used to investigate the physical properties of semiconductors.^{1–3} They are based on the nondestructive detection of heat generated by nonradiative recombination of photoexcited carriers. Various non-contact photothermal techniques, such as photoacoustic detection,^{1,4} infrared radiometry,⁵ and photothermal deflection,^{6,7} have been investigated. However, these methods are not suitable for characterizing semiconductors—particularly, for low concentrations of defects or impurities—owing to their low sensitivities. In the past, we developed a piezoelectric photothermal method for investigating the optical and electronic properties by detecting heat and elastic waves using a piezoelectric transducer attached to the rear surface of a sample.⁸ Placing the piezoelectric transducer in contact with the

sample provided advantages such as high-sensitivity detection and the ability to perform low-temperature measurements using a cryostat. The electron transitions in the thin single quantum well of 10 nm and the low concentration of the deep defect levels around 10^{12} – 10^{15} cm^{−3} were well resolved by this technique.^{9,10} However, this spectroscopic methodology is not helpful for defect distribution mapping in semiconductors. Contacting a piezoelectric transducer may also cause contamination and defects in the sample. Intense and fine-resolution illumination and non-contact detection are necessary for such mapping.

Interferometry has been used to measure surface displacement and can be applied to photothermal methods.^{11–13} In homodyne interferometry, the surface displacement is estimated according to the phase difference between the excitation and probe beams.^{12–14}

In contrast, in heterodyne interferometry,^{15,16} when two probe beams divided by a polarized beam splitter with frequencies f_1 and f_2 are mixed, a beat with a frequency of $f_b = |f_1 - f_2|$ is formed. If the surface expansion changes the optical path length, the phase of the beat changes, and the surface displacement can be estimated using this phase shift of beat. This technique allows high-precision and high-sensitivity measurements because the phase shift of the beat is unaffected by the fluctuation of the signal intensity.

Takamatsu *et al.* reported the photoacoustic displacement (PAD) method, which is a laser heterodyne interferometric method for measuring surface displacement.^{17–19} They investigated the lattice damage in the surface layers of ion-implanted Si wafers.^{20,21} However, they fixed the modulation frequency of the excitation beam (f_{ex}) to 87 kHz. Using a lock-in amplifier, they mixed the oscillator frequency with the fluctuation noise and canceled out the noise component. However, such a high frequency resulted in a small displacement, and the detection was difficult.

f_{ex} is an essential factor for investigating the thermophysical properties of semiconductors. This is because the thermal diffusion length (L) is given as $L = \sqrt{\kappa/\rho c \pi f_{ex}}$, where κ represents the thermal conductivity, ρ represents the density, and c represents the specific heat. Hence, the displacement is larger when f_{ex} is smaller, making it easier to detect. Moreover, thermal diffusivity can be estimated from the measurement of the f_{ex} dependence of the surface displacement since the photothermal signals depend on L .^{3,4,22}

The photothermal method can be used to investigate a nonradiative recombination center in semiconductor, such as defects and deep-lying electronic levels. Mapping of the photothermal signal was reported using atomic force microscopy (AFM)²³ and photothermal beam deflection (PBD).²⁴ The reported AFM and PBD mappings cannot measure the time variation of surface displacement. The time variation of the displacement includes information on physical properties such as optical absorption, carrier generation, diffusion, recombination, and thermal diffusion, which may be useful for evaluating defects.

Although photoluminescence mapping and microwave photoconductivity decay (μ -PCD) mapping have been used to examine the defect distributions in semiconductors,^{25–29} they cannot be applied to materials having low luminous efficiencies or very short carrier lifetimes.

We then developed a laser heterodyne photothermal displacement (LH-PD) method for quantitative detection of surface displacement and its time variation at various f_{ex} . Mapping the LH-PD signal can reveal the distributions of nonradiative recombination centers introduced by heavy-metal contamination in semiconductors. Herein, we discuss the usefulness of the LH-PD methodology and its application to defect mapping in semiconductors.

II. EXPERIMENTAL

The experimental configuration of the LH-PD measurement system is shown in Fig. 1. A laser diode (LD) with a wavelength of 808 nm was used as the excitation beam. Its intensity was modulated by an oscillator (OSC) using an LD driver. When a modulated excitation beam was irradiated on the sample surface, the light-absorbed area was periodically heated by the generated heat owing

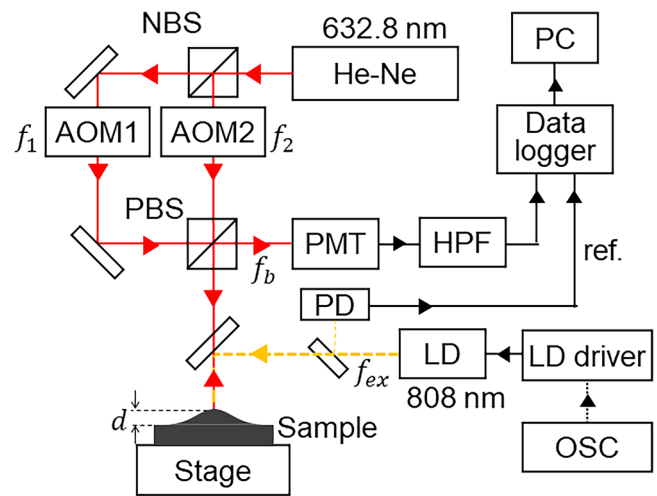


FIG. 1. Block diagram of the experimental configuration.

to the nonradiative recombination of the photoexcited carriers. The periodic surface thermal expansion was measured via the heterodyne interferometric method using a Mach-Zehnder interferometer. A stabilized He-Ne laser (632.8 nm, 5 mW) was used as the probe beam, which was separated into two equivalent beams using a nonpolarizing cube beam splitter (NBS). The frequencies of the beams were set as f_1 and f_2 using acousto-optic modulators (AOMs). The beam with frequency f_1 (reference beam) was passed through a polarizing beam splitter (PBS). The beam with frequency f_2 (measuring beam) was passed through a PBS and focused on the sample surface. The beam that returned from the sample surface was reflected at 90° by the PBS because it was polarized in a perpendicular direction (s-polarized). When the reference and measuring beams were mixed after passing the PBS, a beat signal with a frequency of $f_b (= |f_1 - f_2| = 80 \text{ kHz})$ was formed and detected by a photomultiplier tube (PMT). The beat signal was recorded by a datalogger (Hioki, Memory HiCorder MR8847) after passing through a high-pass filter (HPF). Simultaneously, part of the excitation beam was detected by a Si photodiode (PD) and recorded by the datalogger as a reference signal.

When the sample surface expanded periodically, the optical path length of the measuring beam changed, resulting in a phase shift of the beat signal. Because the incident and reflected beams passed through the same optical path, the relationship between the surface displacement (d) and the phase shift ($\Delta\phi$) is expressed as follows:

$$d = \frac{\lambda}{2} \times \frac{\Delta\phi}{2\pi}, \quad (1)$$

where λ represents the wavelength of the probe beam. $\Delta\phi$ is calculated from $\Delta\phi = 2\pi \times \Delta t / T_{\text{cycle}}$, where T_{cycle} is the cycle. Δt is the time difference between the excitation beam turned on and off and calculated from the number of beat wave peaks. The time variation of several hundred cycles is recorded and averaged. Because λ of

the probe beam was 632.8 nm, we could measure the surface displacement in the range of 0–316.4 nm.

The most distinctive feature of the heterodyne interferometer used in this study is that the frequencies of the probe (f_b) and excitation (f_{ex}) beams could be independently selected. f_{ex} could be changed from 0.1 to 10 kHz while maintaining f_b at 80 kHz. Additionally, the time-dependent surface displacement could be uniquely determined, because the beat was recorded as a function of time using the datalogger.

The sample was placed on the XYZ stage. The excitation and detection beams were scanned by manipulating the stage, and surface-displacement mapping was performed. Our measurement system could measure a maximum area of $2 \times 2 \text{ cm}^2$ with a minimum spacing of 10 nm. The spot sizes (diameters) of the excitation and detection beams were 7.8 and $36 \mu\text{m}$ measured by the beam profiler, respectively.

The physical parameters of the samples used in this study are presented in Table I. *p*-type Si (*p*-Si) and semi-insulating (SI)-GaAs substrate samples were cut from Czochralski- and vertical gradient freeze-grown wafers, respectively. Because the physical properties of Si and GaAs have been widely reported, we assumed that they were the most appropriate materials for validating our experimental system and the subsequent model calculations. The excitation beam intensity of the *p*-Si and SI-GaAs samples was set to 108.0 and 47.6 mW, respectively, as appropriate conditions considering the temperature rise and the measurable displacement.

We also prepared an Fe-contaminated *p*-Si sample ($12 \times 15 \text{ mm}^2$) to demonstrate the usefulness of LH-PD mapping for intentionally introduced defects. Recombination centers due to Fe contamination have been reported.^{30,31} We annealed the *p*-Si sample with an Fe plate on it at 600 °C for 30 min to contaminate it with Fe. The Fe plates were rectangular and triangular. The

rectangular size was $4.0 \times 4.2 \text{ mm}^2$, and the length of the three sides of the triangle was 5.7, 6.0, and 8.2 mm. After removing an Fe plate, an area of 10 mm^2 was measured at 0.15-mm intervals, which is 5184 points. f_{ex} was set at 380, 500, or 2000 Hz during mapping.

We also performed μ -PCD mapping of the same Fe-contaminated *p*-Si sample to compare mapping between displacement and lifetime. An area of $12 \times 15 \text{ mm}^2$ was measured at 0.5-mm intervals using LTA-1510EP (KOBELCO Research Institute, Inc.). 0.5-mm intervals were the minimum spacing that could be set. The excitation beam wavelength and diameter were 904 nm and 2 mm, respectively.

To confirm the accuracy of the measured surface displacement, we used a piezoelectric stage (piezo-stage) controlled with an accuracy of 1 nm. A mirror was attached to the piezo-stage instead of the sample, and the displacement was measured by moving it. The observed displacement from the phase shift of the LH-PD measurements based on Eq. (1) was precisely equal to the artificially set travel distance of the piezo-stage. Therefore, we confirmed that the experimental system was constructed correctly and that the observed displacement was reasonable for discussion.

Simultaneously, we measured the LH-PD signal intensity by changing the excitation-beam intensity to confirm the linearity of the observed signal. This is because the displacement within the elastic limit was proportional to the excitation-beam intensity. The measured displacement was proportional to the incident power of the excitation beam, and the minimum observed displacement of the *p*-Si sample was 0.04 nm when the excitation-beam power was 0.36 mW. These results indicate that a displacement of less than 1 nm can be measured using the present system.

III. THEORETICAL MODEL FOR CALCULATING SURFACE DISPLACEMENT

The following series of calculations were conducted using COMSOL Multiphysics® software.³² We used cylindrical coordinates to estimate the surface displacement theoretically, as shown in Fig. 2(a). When the carriers are photoexcited in semiconductors, they diffuse and recombine. The surface displacement observed in LH-PD is due to the heat generated by the nonradiative recombination of such carriers. Therefore, the heat-diffusion equation and carrier continuity equations should be solved simultaneously. In this case, the heat-diffusion equation is expressed as

$$\frac{\partial T(t, r, z)}{\partial t} = \frac{\kappa}{\rho c} \left(\frac{\partial^2 T(t, r, z)}{\partial r^2} + \frac{1}{r} \frac{\partial T(t, r, z)}{\partial r} + \frac{\partial^2 T(t, r, z)}{\partial z^2} \right) + \frac{Q(t, r, z)}{\rho c}, \quad (2)$$

where T represents the temperature, t represents time, r represents the radial coordinate, z represents the axial coordinate, ρ represents the density, c represents the specific heat, κ represents the thermal conductivity, and Q represents the incident heat power density.

As shown in Fig. 2(a), two types of boundary conditions were introduced for heat transfer to the ambient environment. We used the Robin boundary conditions³³ on the light-illuminated surface and side of the cylinder, where the heat flow from the sample to

TABLE I. Sample specifications and physical properties for calculations.

		<i>p</i> -Si	SI-GaAs	
Thickness	μm	400	500	
Carrier lifetime	$2.5 \mu\text{s}$	4 ns		This work
Surface recombination velocity	cm/s	1000	1000	This work
Optical absorption coefficient	cm^{-1}	922	7372	Refs. 37 and 38
Reflectance of excitation beam	%	32.8	32.6	Refs. 38 and 39
Carrier diffusion coefficient	cm^2/s	31.6	214.7	Ref. 37
Bandgap energy	eV	1.12	1.42	Ref. 37
Thermal conductivity	W/m K	156	46	Ref. 37
Specific heat	J/g K	0.713	0.327	Ref. 37
Density	g/cm^3	2.33	5.32	Ref. 37
Thermal expansion coefficient	$\times 10^{-6} \text{ K}^{-1}$	2.59	5.75	Ref. 37
Poisson's ratio		0.278	0.31	Refs. 35 and 40
Young's modulus	GPa	130	85.5	Ref. 37

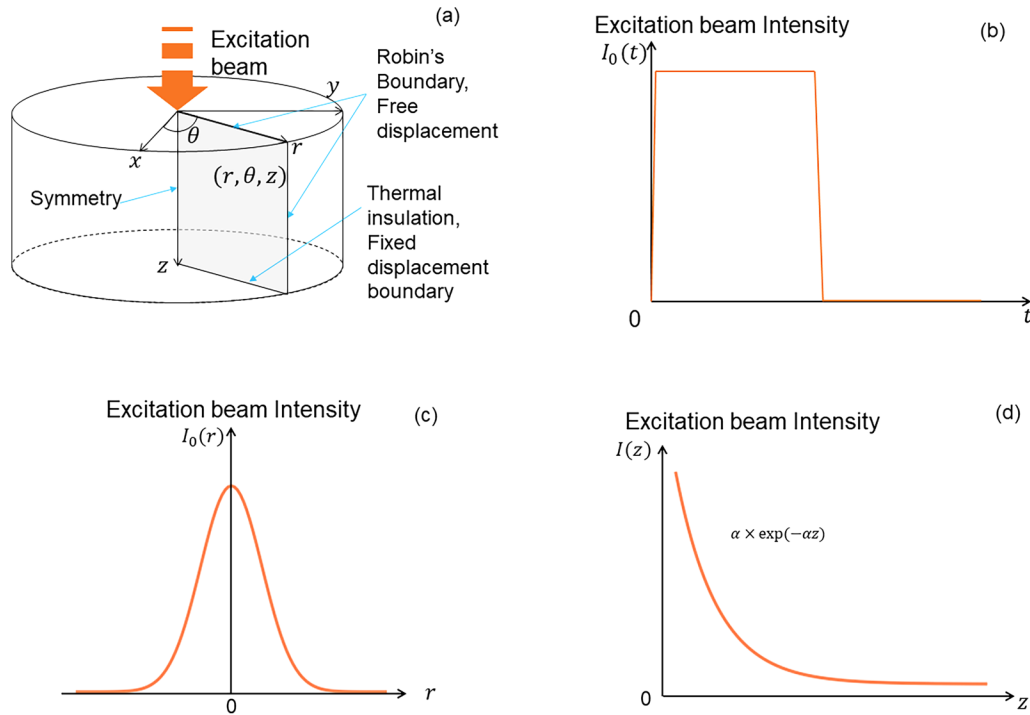


FIG. 2. (a) Cylindrical coordinates for the calculation model. The light-illuminated surface and the sides of the cylinder are under Robin's boundary conditions and free displacement boundary conditions. The boundary conditions of the opposite side of the light-illuminated surface include thermal insulation and fixed displacement. (b) Time variation, (c) the profile in the radial direction, and (d) the depth profile along the z -direction of the excitation-beam intensity.

the ambient temperature was proportional to the surface temperature. In contrast, the thermal insulation boundary condition was used on the opposite side of the light-illuminated surface. This is because the thermal conductivities of the stage made of quartz glass were sufficiently low. These conditions are shown in Fig. 2(a).

Three heat sources are considered for $Q(r, z, t)$ in Eq. (2).³⁴ The first is instantaneous heat generation due to the intra-band nonradiative relaxation of carriers excited above the bandgap. The heat power density of this process Q_D ³⁴ is expressed as

$$Q_D = \frac{\alpha(h\nu - E_g)}{h\nu} I_0(r, t) \exp(-\alpha z), \quad (3)$$

where α represents the optical absorption coefficient for photons of energy $h\nu$, E_g represents the bandgap, and $I_0(r, t)$ (W/cm^2) represents the excitation-beam intensity at the surface. The time variation and intensity distribution of the excitation beam $I_0(r, t)$ are shown in Figs. 2(b) and 2(c). The Gaussian beam profile is assumed to be in the radial direction for the r coordinates of the excitation beam. The time variation and the depth profile along the z -direction are also shown in Fig. 2(d). The second heat source considered is the excess carrier recombination that occurred after the diffusion of carriers over a certain distance $(D\tau)^{1/2}$, where D is the carrier diffusion coefficient and τ represents the carrier lifetime.

The corresponding heat power density Q_{NRR} ³⁴ is expressed as

$$Q_{NRR} = \frac{E_g}{\tau} n(r, z, t), \quad (4)$$

where $n(r, z, t)$ represents the concentration of photoexcited carriers. The third heat source is nonradiative carrier recombination at the sample surface. We assume that the photoexcited carriers are expected to release a total energy that is equivalent to the bandgap energy even in the case of surface recombination. The corresponding heat power density Q_{SR} ³⁴ is expressed as

$$Q_{SR} = E_g v [(\delta(z) + \delta(z + l_s) + \delta(r + w_s))] n(r, z, t), \quad (5)$$

where v represents the carrier surface recombination velocity at the surface, l_s represents the thickness, and w_s represents the radius of the sample. The three terms in Eqs. (3)–(5) are used to calculate the temperature $T(r, z, t)$ in the sample as follows:

$$Q(r, z, t) = Q_D + Q_{NRR} + Q_{SR}. \quad (6)$$

Because the heat sources as a function of the carrier concentration are included in the heat-diffusion equation, the concentration of photoexcited carriers $n(r, z, t)$ should be calculated using

the carrier-diffusion equation,

$$\frac{\partial n}{\partial t} = D \left(\frac{\partial^2 n}{\partial r^2} + \frac{1}{r} \frac{\partial n}{\partial r} + \frac{\partial^2 n}{\partial z^2} \right) - \frac{n}{\tau} + \frac{\alpha I_0(r, t)}{h\nu} \exp(-\alpha z) - vn[\delta(z) + \delta(z + l_s) + \delta(r + w_s)]. \quad (7)$$

The surface recombination at the light-irradiated surface, the side of the cylinder, and the opposite side of the light-illuminated surface was considered.

After the temperature was calculated by solving the thermal diffusion equation, the thermal stress and displacement were calculated from the elastic equation. We calculated the boundary conditions by fixing the displacement on the opposite side of the light-irradiated surface, which was in contact with the sample stage. As the thickness is reduced, the surface heating induces bending in the sample in addition to the localized thermal expansion.³⁵ However, the edge of the sample was fixed by the sample holder in our system, and then the sample did not bend. Thus, our boundary condition is reasonable. The displacement at the light-irradiated surface and the side of the cylinder was assumed to be free. Since the diameter of the excitation beam was smaller than the probe beam, a final displacement was calculated by a weighted average with the area where the detection beam was irradiated. Specifically, the weights were the product of the Gaussian distribution of the probe beam intensity and the micro-area of the probe beam divided into concentric or hollow circles depending on the distance from the center.

IV. RESULTS AND DISCUSSION

The time variations in the surface displacement are shown in Fig. 3. The measured data for the *p*-Si and SI-GaAs samples are represented by red and blue circles, respectively. The experimental results were averaged over 400 cycles. The surface displacement increased exponentially when the excitation beam was turned on. Subsequently, the signal decreased when the excitation beam was turned off. The calculation results were also plotted as red and blue curves for the *p*-Si and SI-GaAs samples, respectively. As shown, the experimental and calculation results agreed well.

Note that Flizikowski *et al.* reported the influence of thermal lens on laser-induced surface displacement.³⁶ The air temperature around the sample surface was calculated, and the phase change of the probe beam due to refractive index change by temperature rise was estimated to consider the thermal lens effect. We confirmed that the thermal lensing effects were minimal and did not change the displacement at all. Moreover, edge effects may increase photothermal signals.³⁸ The edge effect was also negligible because we measured at the center of the sample, where the sample size was sufficiently larger than the sum of the carrier and thermal diffusion lengths.

In our fitting analysis, literature values for the optical absorption coefficient, reflectance of the excitation beam, carrier lifetime, carrier diffusion coefficient, bandgap energy, thermal conductivity, specific heat, density, thermal expansion coefficient, Poisson's ratio, and Young's modulus were used as shown in Table I.^{35,37–40} For the lifetime of *p*-Si, we used 2.5 μ s, which was measured via the μ -PCD method for the present sample. The surface recombination velocities of Si and GaAs were assumed to be 1000 cm/s, which is generally used for solar-cell simulations. For GaAs, we considered

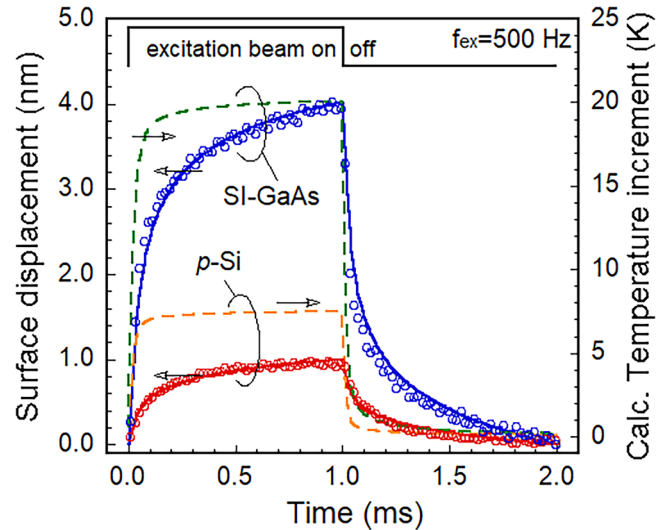


FIG. 3. Time variations of the surface displacement for the *p*-Si and SI-GaAs samples. f_{ex} and f_b were 500 Hz and 80 kHz, respectively. Circles and solid curves represent the experimental and calculation results, respectively. The dashed curves represent the calculated temperatures at the center and the surface. The experimental results were averaged over 400 cycles.

the lifetime as a fitting parameter to match the experimental and calculation results because it is shorter than the detection limit of μ -PCD. The best-fit lifetime was 4 ns. The literature value for the lifetime of GaAs was 10 ns³⁷; thus, the fitted and literature lifetime values were both on the order of nanoseconds. Hence, we considered that the fitting results were reasonable. Because the time variation of the displacement in the calculation is sensitive to slight changes in the physical parameters, it becomes useful for mapping the nonradiative recombination centers in the sample.

The observed maximum surface displacements of the *p*-Si and SI-GaAs samples were 1.0 and 4.0 nm, respectively. Although the excitation beam intensity of the SI-GaAs samples was smaller, a larger displacement was observed for the SI-GaAs sample. Meanwhile, the calculated maximum temperature increment at the center in the excitation beam of the *p*-Si and SI-GaAs samples was 7.5 and 20.1 K, respectively, as shown by dashed curves in Fig. 3. A larger optical absorption coefficient and linear expansion coefficient and lower thermal conductivity result in higher temperature and a larger displacement. Therefore, the observed surface displacement of the SI-GaAs sample was larger than that of the *p*-Si sample, as shown in Table I.

The time variation of the displacement for the *p*-Si sample was slower than that for the SI-GaAs sample, as shown in Fig. 3. Generally, the time variation of the temperature that causes the surface displacement should be faster for higher thermal conductivity. For example, in the micro-time-domain thermoreflectance method, where the temperature change is determined according to the reflectance change of the Al film, the time variation of the signal intensity is faster when the thermal conductivity is higher.^{41,42} This was not the case in our experimental results. The observed time variation of the displacement cannot be explained by

only the changes in the thermal properties without considering the carriers. In addition, although the calculations indicated that the decay time of the displacement was shorter when the optical absorption coefficient was larger, the experimental results could not be explained by the difference between the optical absorption coefficients of Si and GaAs. Carrier diffusion and recombination should also be considered. Therefore, we performed additional calculations considering the carrier generation, diffusion, and recombination, as mentioned in Sec. III. As a result, experimental results were well reproduced as shown in Fig. 3.

Flizikowski *et al.* measured the thermal conductivities of metals according to the time variation of the surface displacement by using a photothermal mirror and homodyne interferometry.¹⁴ However, carrier diffusion is not considered in their theoretical model.¹⁴ The surface displacement of the metal is described by thermal diffusion with an instantaneous heat source. Light is absorbed in the thin surface layer of the sample, and heat is instantaneously generated in the metals. Consideration of carrier diffusion is essential for semiconductors because the experimental time variation of the surface displacement cannot be explained using only thermal and optical parameters, as mentioned previously.

Figure 4 shows the time variations of surface displacement of *p*-Si when the values of f_{ex} were 380, 500, and 3600 Hz. The experimental results were well reproduced by calculations for each f_{ex} . All experimental and calculated results were normalized at each maximum value. The maximum surface displacements for f_{ex} of 380, 500, and 3600 were 1.5, 1.0, and 0.7 nm, respectively. Changing f_{ex} varies the thermal diffusion length as mentioned

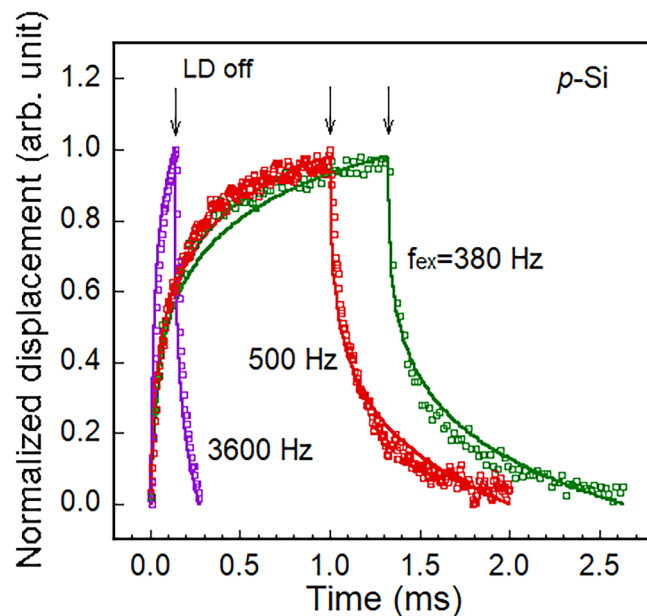


FIG. 4. Time variations of the surface displacement for the *p*-Si sample. f_{ex} was 380, 500, and 3800 Hz and f_b was 80 kHz. Squares and solid curves represent the experimental and calculation results, respectively. The surface displacement was normalized at each maximum value.

above. By measuring and fitting the time variation with various f_{ex} , it may be possible to calculate the thermal diffusivity.

We performed surface-displacement mapping measurements for the *p*-Si sample. Note that there was a margin of the sample about 1 mm outside the mapping measurement area. Therefore, we could also neglect the edge effects because the sum of thermal and carrier diffusion length was sufficiently smaller than 1 mm. Because a uniform mapping result was obtained for the *p*-Si sample, this sample was annealed for 30 min at 600 °C with an Fe plate. Figure 5 shows the surface-displacement mapping when f_{ex} was 2000 Hz. We observed rectangular and triangular shapes as the differences in surface displacement, as shown in Fig. 5. Besides, these shapes could not be observed via optical microscopy with a resolution of 10 μ m. The displacement mapping at f_{ex} of 2000 Hz observed triangular and rectangular shapes more clearly than those of 380 and 500 Hz. It is noted that the scanning depth from the surface can be considered equal to the thermal diffusion length. Increasing f_{ex} leads to shortening scanning depth. The results in Fig. 5 were appropriate because the heat treatment will cause iron atoms to diffuse from the surface to form nonradiative recombination centers.

The surface displacement inside the triangle increased, while that inside the rectangle decreased. On the other hand, there was no significant difference in the time variation of the displacement between the inside and outside of the triangle or the rectangle. This may have been due to the differences in the recombination centers, such as the neutral and charged interstitial Fe and Fe-B pairs,^{30,31} but further discussion is needed.

We also performed lifetime mapping of same Fe-contaminated *p*-Si sample using μ -PCD as shown in Fig. 6. Although a change in lifetime was observed, the rectangular and triangular shapes could not be identified. The μ -PCD method measures microwave (10 GHz) reflection by photo-excited carriers formed by a 904 nm laser diode.

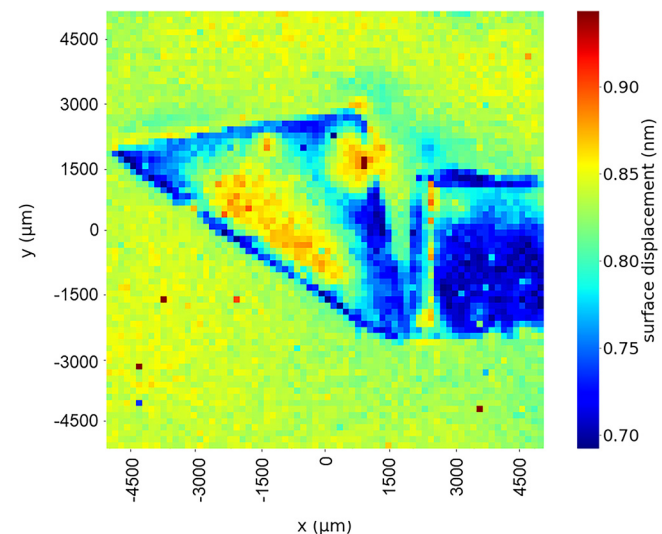


FIG. 5. Displacement mapping results for an Fe-contaminated *p*-type Si sample. An area of 10 mm² was measured at 0.15-mm intervals, which is 5184 points. Large- and small-displacement locations are shown in red and blue, respectively. f_{ex} and f_b were 2000 Hz and 80 kHz, respectively.

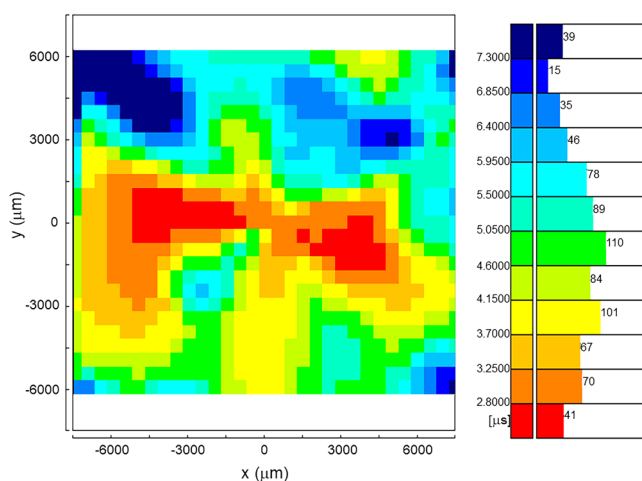


FIG. 6. Lifetime mapping results for an Fe-contaminated *p*-type Si sample using the μ -PCD method. An area of $12 \times 15 \text{ mm}^2$ was measured at 0.5-mm intervals, which is 775 points. Longer- and shorter-lifetime locations are shown in blue and red, respectively. Wavelength of the excitation beam and diameter was 904 nm and 2 mm, respectively.

The penetration depth of microwaves is about 2 mm. Thus, there is no resolution in the depth direction. These results suggest that the LH-PD technique is highly sensitive to nonradiative recombination centers.

Finally, we compared the specifications of present LH-PD with those of reported photothermal signal mappings such as by PBD,²⁴ PAD,¹⁷ and AFM.²³ The spatial resolution of the LH-PD method was determined by the spot size of the probe beam and was expected to be $36 \mu\text{m}$. As for PBD and PAD, spatial resolution was expected to be comparable to LH-PD because it was determined by the spot size of the probe beam. The spatial resolution of the cantilever for AFM was an order of nanometers. On the other hand, the measurable range of AFM is several tens of micrometers, which is narrower than that of LH-PD. LH-PD should be used for wider areas from micrometers to centimeters, while AFM should be used for fine measurements in narrower areas from nanometers to micrometers.

The typical scanning speed was 7.5 s per point for our LH-PD. Although no information about scanning speed was obtained for AFM,²³ PBD,²⁴ and PAD,¹⁷ our mapping measurements may not be so fast compared to other methods. This is because the LH-PD records the time variation of the surface displacement at each scanning point. On the other hand, PAD,¹⁷ PBD,²⁴ and AFM²³ cannot measure it. It is noted that by analyzing the waveform of the time-dependent displacement obtained by the present LH-PD method, we can discuss the change in physical parameters around the nonradiative recombination centers. This is beneficial for analyzing nonradiative recombination centers.

V. CONCLUSION

We developed an LH-PD technique and detected subnanometer surface displacement. The time variations of the surface

displacement of *p*-Si and Si-GaAs samples could be explained by considering the optical absorption, carrier diffusion, and thermal parameters. Measurements with different thermal diffusion lengths and appropriate LH-PD signals could be performed because f_{ex} could be selected independently of the frequency of the beat signal of the probe beam. In addition, if we change f_{ex} , thermal diffusivity could be estimated by curve fitting. Incidentally, when positions of excitation and probe beams are intentionally separated, we can evaluate the in-plane or local thermal conductivity.

We also performed surface-displacement mapping of an Fe-contaminated *p*-Si sample. The locations of the nonradiative recombination centers were clearly indicated by the displacement difference. The LH-PD method was sensitive to nonradiative recombination centers, and the same patterns could not be measured via lifetime mapping using the μ -PCD method. The mechanism underlying nonradiative recombination centers that increase or decrease the surface displacement should be investigated in the future.

In this study, the locations of nonradiative recombination centers were observed in a two-dimensional plane. It may be possible to map the nonradiative recombination centers in three dimensions by varying f_{ex} . When f_{ex} is selected, the thermal diffusion length is changed, making it possible to measure the measurement range in the thickness direction.

ACKNOWLEDGMENTS

We thank Dr. K. Nishioka and Dr. Y. Ota (University of Miyazaki) for their assistance with the numerical calculations. This study was supported by JSPS KAKENHI (Grant Nos. JP20H05649 and JP18K04876) and a Grant-in-Aid for JSPS Research Fellows (Grant No. JP21J22312).

AUTHOR DECLARATIONS

Conflict of Interest

The authors have no conflict of interest to disclose.

DATA AVAILABILITY

The data that support the findings of this study are available from the corresponding author upon reasonable request.

REFERENCES

- ¹A. Rosencwaig and A. Gersho, *J. Appl. Phys.* **47**, 64 (1976).
- ²W. Jackson and N. M. Amer, *J. Appl. Phys.* **51**, 3343 (1980).
- ³S. Horita, H. Konishi, N. Miyabo, and T. Hata, *Jpn. J. Appl. Phys.* **33**, 3238 (1994).
- ⁴X. Wang, H. Hu, and X. Xu, *J. Heat Transfer* **123**, 138 (2001).
- ⁵A. Mandelis, J. Batista, and D. Shaughnessy, *Phys. Rev. B* **67**, 205208 (2003).
- ⁶W. B. Jackson, N. M. Amer, A. C. Boccara, and D. Fournier, *Appl. Opt.* **20**, 1333 (1981).
- ⁷M. Sumiya, K. Fukuda, H. Iwai, T. Yamaguchi, T. Onuma, and T. Honda, *AIP Adv.* **8**, 115225 (2018).
- ⁸T. Ikari and A. Fukuyama, in *Progress in Photothermal and Photoacoustic Science and Technology. Semiconductors and Electronic Materials*, edited by A. Mandelis (SPIE, Bellingham, WA, 2000), p. 145.
- ⁹T. Ikari, K. Imai, and A. Ito, *Appl. Phys. Lett.* **82**, 3302 (2003).
- ¹⁰A. Fukuyama, A. Memon, K. Sakai, Y. Akashi, and T. Ikari, *J. Appl. Phys.* **89**, 1751 (2001).

- ¹¹J. T. Fanton and G. S. Kino, *Appl. Phys. Lett.* **51**, 66 (1987).
- ¹²S. A. Carp and V. Venugopalan, *J. Biomed. Opt.* **12**, 064001 (2007).
- ¹³T. Požar, P. Gregorčič, and J. Možina, *Appl. Phys. B* **105**, 575 (2011).
- ¹⁴G. A. S. Flizikowski, O. A. Capeloto, V. G. Camargo, B. Anghinoni, M. L. Baesso, L. C. Malacarne, M. P. Belançon, T. Požar, and N. G. C. Astrath, *Opt. Express* **28**, 7116 (2020).
- ¹⁵N. A. Massie, R. D. Nelson, and S. Holly, *Appl. Opt.* **18**, 1797 (1979).
- ¹⁶D. C. Su, M. H. Chiu, and C. Der Chen, *J. Opt.* **27**, 19 (1996).
- ¹⁷H. Takamatsu, Y. Nishimoto, and Y. Nakai, *Jpn. J. Appl. Phys.* **29**, 2847 (1990).
- ¹⁸S. Sumie, H. Takamatsu, Y. Nishimoto, T. Horiuchi, H. Nakayama, T. Kanata, and T. Nishino, *Jpn. J. Appl. Phys.* **31**, 3575 (1992).
- ¹⁹S. Sumie, H. Takamatsu, Y. Nishimoto, Y. Kawata, T. Horiuchi, H. Nakayama, T. Kanata, and T. Nishino, *J. Appl. Phys.* **74**, 6530 (1993).
- ²⁰S. Sumie, H. Takamatsu, T. Morimoto, Y. Nishimoto, Y. Kawata, T. Horiuchi, H. Nakayama, T. Kita, and T. Nishino, *J. Appl. Phys.* **76**, 5681 (1994).
- ²¹H. Takamatsu, S. Sumie, T. Morimoto, Y. Kawata, T. Muraki, and T. Hara, *J. Appl. Phys.* **78**, 1504 (1995).
- ²²M. D. Dramićanin, P. M. Nikolić, Z. D. Ristovski, D. G. Vasiljević, and D. M. Todorović, *Phys. Rev. B* **51**, 14226 (1995).
- ²³K. Hara and T. Takahashi, *Appl. Phys. Express* **5**, 022301 (2012).
- ²⁴J. Younes, Z. Harajili, M. Soueidan, D. Fabregue, Y. Zaatar, and M. Kazan, *J. Appl. Phys.* **127**, 173101 (2020).
- ²⁵D. Kiliani, G. Micard, B. Steuer, B. Raabe, A. Herguth, and G. Hahn, *J. Appl. Phys.* **110**, 054508 (2011).
- ²⁶J. Härkönen, E. Tuovinen, Z. Li, P. Luukka, E. Verbitskaya, and V. Eremin, *Mater. Sci. Semicond. Process.* **9**, 261 (2006).
- ²⁷E. Higashi, M. Tajima, N. Hoshino, T. Hayashi, H. Kinoshita, H. Shiomi, and S. Matsumoto, *Mater. Sci. Semicond. Process.* **9**, 53 (2006).
- ²⁸H. Sugimoto, M. Inoue, M. Tajima, A. Ogura, and Y. Ohshita, *Jpn. J. Appl. Phys.* **45**, L641 (2006).
- ²⁹K. Lauer, A. Laades, H. Übensee, H. Metzner, and A. Lawerenz, *J. Appl. Phys.* **104**, 104503 (2008).
- ³⁰A. A. Istratov, H. Hieslmair, and E. R. Weber, *Appl. Phys. A: Mater. Sci. Process.* **69**, 13 (1999).
- ³¹M. Itsumi, *Appl. Phys. Lett.* **63**, 1095 (1993).
- ³²COMSOL AB, COMSOL Multiphysics® v. 5.6, see www.comsol.com. Stockholm, Sweden.
- ³³H. P. Langtangen, *Computational Partial Differential Equations*, 2nd ed. (Springer, Berlin, 1999), p. 260.
- ³⁴A. Pinto Neto, H. Vargas, N. F. Leite, and L. C. M. Miranda, *Phys. Rev. B* **40**, 3924 (1989).
- ³⁵P. P. Gonzalez-Borrero, G. V. B. Lukasiewicz, V. S. Zanuto, N. G. C. Astrath, and L. C. Malacarne, *J. Appl. Phys.* **121**, 195101 (2017).
- ³⁶G. A. S. Flizikowski, B. Anghinoni, J. H. Rohling, M. P. Belançon, R. S. Mendes, M. L. Baesso, L. C. Malacarne, T. Požar, S. E. Bialkowski, and N. G. C. Astrath, *J. Appl. Phys.* **128**, 044509 (2020).
- ³⁷S. M. Sze and K. K. NG, *Physics of Semiconductor Devices*, 3rd ed. (John Wiley & Sons, Hoboken, 2007), pp. 665–790.
- ³⁸*Handbook of Optical Constants of Solids*, edited by E. D. Palic (Academic Press, Orlando, 1985), p. 439, 565, 729, and 760.
- ³⁹D. E. Aspnes and A. A. Studna, *Phys. Rev. B* **27**, 985 (1983).
- ⁴⁰L. Gan, B. Ben-Nissan, and A. Ben-David, *Thin Solid Films* **290–291**, 362 (1996).
- ⁴¹M. Nomura, Y. Kage, J. Nakagawa, T. Hori, J. Maire, J. Shiomi, R. Anufriev, D. Moser, and O. Paul, *Phys. Rev. B* **91**, 205422 (2015).
- ⁴²X. Huang, D. Ohori, R. Yanagisawa, R. Anufriev, S. Samukawa, and M. Nomura, *ACS Appl. Mater. Interfaces* **12**, 25478 (2020).